Characterising uncertainty and external disturbance sources in wave tank experiments for wave energy converter modelling

Mahdiyeh Farajvand, Demián García-Violini, John V. Ringwood

Abstract—**Uncertainty, whether inherent to the dynamical system under study or due to external factors, is intrinsic to experimental wave tank tests of wave energy converter (WEC) devices. In order to obtain a representative WEC model from wave tank experiments, it is crucial to identify and characterise nonlinearities, uncertainty, and external disturbance affecting the experimental data, to understand the level of data contamination at different operating conditions of the system, and to apply the proper methodologies to compensate for those effects, where appropriate. To this aim, the current study anlyses wave tank data from an experimental campaign on a 1/20 scale Wavestar prototype device to identify a range of linear WEC models, using force-input experiments at various levels, with a focus on the identification and quantification of parameters that may cause uncertainty in the WEC model. To this end, the analysed phenomena are classified into electromechanical, hydrodynamic, and structural (support) parts of the test setup. Effective data pre-processing and post-processing steps, to mitigate noise and disturbances, as well as preserving the physical system behaviour, are applied to identifying representative linear WEC models, which serves as staring point for robust WEC controller synthesis. Thus, careful estimation of representative models and a associated uncertainty region overcomes the limitations of a single linear model by covering the complete operational space of the device.**

Index Terms—**Wave energy converter (WEC), Experimental WEC model, Uncertainty quantification, Linearised WEC models**

I. Introduction

CONSIDERABLE testing and modeling are required in order to fully realise, efficiently develop, and successfully industrialise wave energy converters (WECs). Mathematical WEC models form the basis of model-based energy maximising control and directly affect the ability of model-based controllers to maximise energy capture. Models capturing the nonlinear dynamics of the entire chain of a WEC best reproduce the accurate behaviour of the device for model-based control and precise power production assessment [1], while models obtained from linear WEC modelling methods can overestimate both motion and power absorption.

Numerical modelling, full-scale measurements, and scaled prototype testing, to mention a few, are various methodologies that can be applied to model WECs and predict the dynamic response. However, there are many nonlinear effects, and diverse factors causing uncertainty, both in the numerical world [2], [3] and physical experiments [4], [5], [6], which need to be identified and quantified for identification of representative WEC models, which are particularly useful for model-based control designs. A range of uncertainty sources in each type of aforementioned experiments is documented in [7]. By way of example, governing equations, numerical methods, and numerical implementations associated with *numerical modelling*; environment, instrumentation, and physical properties of the fluid associated with *full-scale tests*; and scaling, model definition, instrumentation and physical properties of the fluid associated with *model tests* are some of the most important uncertainty sources [5], [7].

Identification of a range of linear WEC models at different operating points (see, for example, [8], [9]), to capture underlying nonlinear behaviour and associated uncertainty, can be considered for obtaining an adequate WEC model, required for implementation of a linear (robust) controllers. Ignoring model uncertainty and external disturbances, for instance in the implementation of a time-invariant (LTI) energy-maximizing control strategy (LiTe-Con), as in study [10], can lead to overestimation of the controller performance, and the deviation trend of the absorbed energy between experimental and simulation results at different sea states. Consequently, neglecting model uncertainty, leading to overestimation of power absorption, has a detrimental impact on the commercial viability of WECs, particularly in control co-design schemes [11].

As mentioned, identification of a range of linear models at different operating points can be used to extract a nominal model, and an associated uncertainty region, that could be used as a basis for a robust WEC controller synthesis, such as articulated in [12], showing improvement of the absorbed energy of the WEC when the controller effectively handles model uncertainty around the nominal model [2], particularly ensuring a possitive absorbed energy in a worst-case

The authors would like to acknowledge funding by Maynooth University of a *John and Pat Hume Doctoral (WISH) Award*, for Mahdiyeh Farajvand, and Science Foundation Ireland through the *Research Centre for Energy, Climate and Marine (MaREI)* under Grant 12/RC/2302_P2, for John Ringwood.

Mahdiyeh Farajvand and John V. Ringwood are with the Center for Ocean Energy Research, Maynooth University, Maynooth W23 F2H6, Ireland (e-mail: Mahdiyeh.Farajvand.2021@mumail.ie, John.Ringwood@mu.ie).

Demián García-Violini is with Departamento de Ciencia y Tecnología, Universidad Nacional de Quilmes, Roque Saenz Peña 352, Bernal B1876, Argentina, Consejo Nacional de Investigaciones Científicas y Técnicas (CONICET), Argentina, and Center for Ocean Energy Research, Maynooth University, Maynooth W23 F2H6, Ireland, (e-mail: ddgv83@gmail.com).

https://doi.org/10.36688/ewtec-2023-paper-376

scenario.

A recent study on representative linear model quantification and uncertainty estimation in a WEC system based on numerical modelling using computational fluid dynamics (CFD) model and the post-processing techniques based on the experiment type has been presented in [2]. Physical wave tank experiments, one of the most important test setups for validation of WEC modelling and control, differ significantly from numerical wave tank (NWT) experiments, in terms of the range of tests that can be performed, and the contamination which can affect the measurements used to determine data-based models. In addition, the range of post-processing techniques which can be applied to the different experimental/numerical domains, to improve the fidelity of the identified models, may differ between domains. As a result, the determination of nominal models and associated uncertainty regions, as well as characterising parameters contaminating the experimental data should be examined carefully.

In this study, a physical wave-tank-based experimental test (lab scale) is considered for the characterisation of representative linear models at different operating points with a specific focus on challenges and uncertainty sources, inherent to experimental settings. Considering the dynamical uncertainty and exogenous (external) noise sources, such as electromechanical parts, structural parts, measurement noise, etc., which contaminate experimental data, uncertainty and noise sources are considered within the two-step force transmission chain (see Section III). Appropriate signal processing techniques are presented to exclude inherent potential nonlinearities and perturbations introduced by the wave tank, which overcome the failure of the previously proposed filtering methods for experimental data using chirp signal excitation [2]. The separation of dynamical behaviour of the WEC from noise and disturbances, introduced by electromechanical and structural parts, and the determination of representative linear WEC models, provide adequate representation (model) to replicate tank-based experiments in simulation environments and avoids overestimation of the device motion. An important application of the proposed study could be obtaining adequate models of the WEC that can be considered for the implementation of the LTI energy-maximizing control strategy, for instance in study [10], and sheds light on the performance deviation between experimental and simulation results described in [10], for the LiTeCon. Even though the signal-to-noise ratio (SNR) has been analysed briefly and accounted as the parameter affecting the control performance in [10], in the present study (considering the same WEC prototype), we go into the details of experimental uncertainty and noise sources that obscure information from the data which has an impact on the accurate dynamic system description and possibly, control performance.

The remainder of this paper is organised as follows. Initially, WEC modelling, including standard linear modelling methods, as well as properties of WEC systems, are presented in Section II. The parameters that may cause uncertainties in WEC model tests are covered in Section III. Next, in Section IV, system identification methods and uncertainty quantification technique has been detailed. Data pre- and post-processing methods for obtaining representative WEC models are presented in Section V. The application case, including wave tank setup, force-to-motion experiments, nonlinearity and noise detection, and system identification results are drawn in Section VI, and, finally, overall conclusions from the study are drawn in Section VIII.

II. WEC MODELING

A. Linear WEC model

Mathematical WEC models, under the assumption of linearity, are commonly studied using linear potential flow theory and the well-known Cummins' equation [13], where the equation of motion of a 1 degree of freedom (DoF) floating structure, in the time domain, can be expressed as:

$$(m + m_\infty)\ddot{y}(t) = f_{\mathrm{ex}}(t) - f_u(t) - k_{\mathrm{h}} y(t) - h_{\mathrm{r}} \star \dot{y}(t), \quad (1)$$

where $m \in \mathbb{R}^+$ is the mass of the device and m_∞ is the added mass at infinite frequency. In Eq. (1), $y(t)$, $\dot{y}(t)$, and $\ddot{y}(t)$ are the device displacement, velocity, and acceleration, respectively, while $f_{\mathrm{ex}}(t)$ is the wave excitation force, produced by the action of incoming waves, and $f_u(t)$ is the control input applied by means of the PTO system. k_{h} is the hydrostatic stiffness, related to buoyancy/gravity forces, and $h_{\mathrm{r}}(t)$ is the radiation impulse response function with $\star$ representing convolution, related to the radiation force, $f_{\mathrm{r}}(t)$, arising from device motion in the fluid.

B. WEC system properties

The properties of stability and passivity are characteristics of a physical WEC system [14] (if the model is not stable and passive, it does not reflect the real system). Stability is a well-known concept for dynamical systems, satisfying the condition of bounded-input bounded-output of the model, and passivity refers to the property of a system where the dissipation of energy occurs solely from external sources, such as the environment or interactions with other systems (the passive system cannot produce energy on its own). The passivity of a linear time-invariant (LTI) system is equivalent to the transfer function being positive for all frequencies [14], or, equivalently the frequency response of the system is contained on the right-hand side of the Nyquist plot. Post-processing methods for passivisation can be used to render a nonpassive system passive [15].

III. PARAMETERS CAUSING UNCERTAINTY IN WEC MODEL TESTS

Many effects can cause uncertainty in WEC model tests which can be classified into three parts: Electromechanical effects, hydrodynamic effects, and structural effects.

A. Electromechanical effects

WEC systems consist of different electromechanical parts which can include sources of nonlinearity, uncertainty, or disturbance that affect the overall performance of the WEC. In a WEC with a linear power take-off (PTO), the electromechanical components include a linear motor, sensors, and a control system. In this system, there is generally a force tracking control loop, which includes a controller, motor, and sensors (Fig. 1), and generates a deviation between the actual force and reference force. The components of the force control loop can contribute to the failure of the correct tracking, as follows:

- *Linear motor*: Dead-zone in a linear motor is considered as a static nonlinearity referring to the operating range of input that produces no or little response in the output. Cogging force, generated primarily due to the interaction between the permanent magnets in the rotor and the stator's magnetic field, is another common nonlinear effect in the linear motor. Due to actuator nonlinearities, the system does not strictly follow a linear relationship between input and output and may cause the failure of a force control loop to accurately generate the target force.
- *Sensors*: Random variations in the sensor readings (unrelated to variations in sensor input) are basically inevitable which corrupt the original data. The signal-to-noise ratio (SNR) is an important parameter that determines the level of the strength of a signal compared to the level of unwanted noise in the signal. The SNR from time domain signals can be obtained by the ratio of the root mean square (RMS) of the signal to the RMS of the noise. In terms of dB, the SNR will be computed as

$$SNR = 20\log(RMS_{signal}/RMS_{noise}) \qquad (2)$$

  Measurement noise can affect the performance of the force control loop, where the control signal is computed based on the error between the reference force and the actual force measured by the force sensor. Another source of error associated with sensors could be saturation in data reading when the data are larger than a measurement limit of the sensor.

B. Hydrodynamic effects

WEC systems are, in general, nonlinear and may contain uncertain sources that may affect the model due to complex hydrodynamic interactions, viscous drag, flow separation, and vortex shedding [16]. Reflections at laboratory scales, as a result of the interaction between the wave and the tank boundaries, is a hydrodynamic effect.

C. Structural effects

The mooring system or mounting structure, depending on the type of WEC, is one of the main sources of uncertainty in experimental test setups. A detailed explanation of the uncertainty in model tests involving mooring lines is discussed in [7]. The mounting structure may experience vibrations during the experiments, specifically for large input amplitude forces applied to a WEC, contributing to artifacts to the experimental data.

D. Force transmission chain

In this study, nonlinearities, uncertainty, and external noise sources, that affect the experimental data, are considered within the two-step force transmission chain, as illustrated in Fig. 1. The two-step chain comprises:

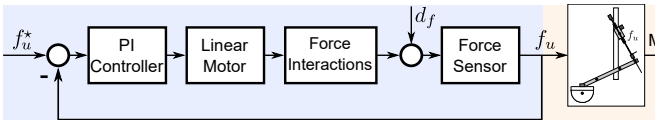

Fig. 1. Two-step chain: $f_u^\star$-to-f_u mapping (step 1) and f_u-to-θ mapping (step 2). Each step in the chain is indicated using shadowed-areas with different colours.

1) *Reference force-to-actual force mapping* (force tracking control): This step is the process of generating the reference input force ($f_u^\star$), for the WEC modelling test which is done via a proportional-integral-based (PI-based) control loop, acting on a linear motor (as illustrated on Fig. 1))
2) *Actual force-to-motion mapping*: This step is the process of generating WEC motion from the applied actual force (f_u) (Fig. 1)).

In Fig. 1, each step of the chain is indicated using shadowed areas, coloured with different colours, while the perturbation signal d_f, represents all the forces considered, for the purpose of the first step of the chain, as exogenous. As mentioned before in Section I, the presented study analyses an experimental-based case study. To clarify the previous explanation, and by way of example, a picture of the prototype and wave basin considered for the case study, as well as their schematic description, including the of PTO system, mounting structure, motion sensors, load cell, and the locations of the centre of the gravity of the device (C_g) and still water level (SWL), are shown in Fig. 2.

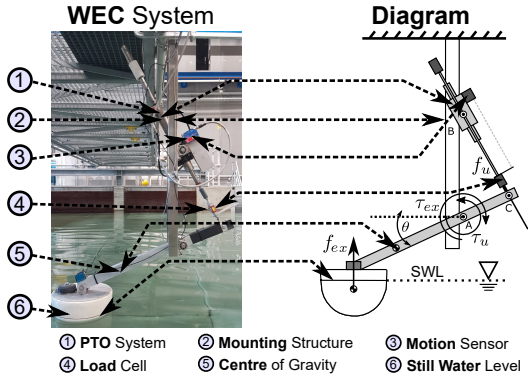

Fig. 2. Components of the experimental WEC system (photograph of the WEC system on the left and schematic diagram on the right)

IV. System Characterisation and Uncertainty Quantification

The linear model for the current study is characterised using standard frequency-domain techniques,

via the so-called empirical transfer function estimate (ETFE). Considering the two-step mapping according to Fig. 1, the mapping $f_u^\star(t) \rightarrow f_u(t)$ ($f_u^\star(t)$ is the reference input force and $f_u(t)$ is the actual input force), and the mapping $f_u(t) \rightarrow \theta(t)$ ($(f_u(t), \theta(t))$ is the input-output pair defined in the time-domain) are calculated. By defining $F_u^\star(j\omega)$, $F_u(j\omega)$ and $\Theta(j\omega)$ as the Fourier transform of $f_u^\star(t)$, $f_u(t)$ and $\theta(t)$, respectively, the ETFEs, $H_1(j\omega)$ and $H_2(j\omega)$, are computed as:

$$H_1(j\omega) = \frac{F_u(j\omega)}{F_u^\star(j\omega)}, \quad H_2(j\omega) = \frac{\Theta(j\omega)}{F_u(j\omega)}. \tag{3}$$

The design of the system input is one important issue in system identification, where a set of input signals should be designed to cover the full input amplitude (dynamical) range of the system, while, at the same time, exciting the system over the frequency range where the system has a significant frequency response (a detailed input signal analysis in a NWT setup has been discussed in [2]). A *chirp signal* is a signal with a time-varying frequency that is of particular interest since a single chirp signal can be designed to cover the complete frequency range of the interest (reducing the number of required experiments compared to single-frequency sinusoidal signals). A linear frequency-modulated chirp signal has the instantaneous frequency $f(t)$ changing with time, as $f(t) = ct + f_0$ (f_0 is the initial frequency and c, the chirp rate). The corresponding time-domain function for a sinusoidal linear chirp can be formulated as:

$$x(t) = A\sin\left(\phi_0 + 2\pi\left(\frac{c}{2}t^2 + f_0 t\right)\right), \quad \text{for } t \geq 0, \tag{4}$$

where, A and ϕ_0 are the amplitude and initial phase of the linear chirp signal, respectively.

V. Data pre- and post-processing

A. Data pre-processing

The output of any experiment that the information is to be extracted commonly is typically contaminated with noise. There are many different types of filters that can be used to reduce the effects of noise and extract desired information from the signal in the time domain. Filtering the noise from chirp-type signals is challenging, due to time-varying contents (frequency). The application of a moving band-pass filter on a chirp signal has been studied in [2], showing the difficulty of correct initialization of the filter output, resulting in unwanted additional transient behaviour artifacts. In this study, a Savitzky-Golay (S-G) filter is applied to chirp-based signals which prove to be particularly useful in smoothing the signal while preserving the shape and details of it.

1) Savitzky–Golay filter

S-G filter [17] is a method of data smoothing based on fitting a local least-squares polynomial to a set of input samples and then replacing each point of a signal by the value of the polynomial at that point. If x[n] is a discrete signal, for a group of 2M + 1 samples (M points to the left and M points to the right of a given data point) centered at n, the polynomial can be computed as:

$$p_n = \sum_{k=0}^{N} a_k n^k \tag{5}$$

where N is the polynomial order, and the polynomial coefficients are computed such that the mean-squared approximation error,

$$\epsilon_N = \sum_{n=-M}^{M} \left(\sum_{k=0}^{N} a_k n^k - x[n]\right)^2 \tag{6}$$

is minimised (frame length is $2M + 1$).

B. Data post-processing

Based on the characteristics of the input/output signals, the physical features of the system, and the level of noise and fluctuations of the ETFE, suitable data post-processing techniques should be applied in order to obtain a representative model. Some post-processing techniques are described as follows:

- *ETFE phase correction*: In order to respect the physical features of the WEC device in terms of passivity (Sec. II-B), data post-processing based on the correction of the resulted ETFE, in terms of phase components to 0° and -180° at the low and high-frequency asymptotes, respectively, and restriction of the system phase within $[-180\ 0]^\circ$ for all frequencies, can be applied.
- *ETFE filtering (Frequency domain)*: Filtering can help to reduce noise in the ETFE and, consequently, retain the true signal representation. A commonly used filter in the time-domain (also has interpretation in the frequency-domain) is moving average method which is based on the calculation of the average of a specified number of adjacent time-domain data points in a sequence.
- *Phase unwrapping of the ETFE*: The phase wrapping problem refers to the jump between the consecutive frequency bins in the phase of the ETFE which can occur due to particular software implementation of the fast Fourier transform, or when there is a high level of noise or distortion in the signal. Phase unwrapping is a post-processing technique used to remove phase discontinuities, for instance, by adding/subtracting 360° to compensate for wrapping problem.

VI. Application case

The system prototype considered in this study is based on the Wavestar system (Fig. 2) [18], [19], which is a well-established and widely recognized WEC standard in the wave energy community. This system essentially consists of a rotational arm connected to a hemispherical floater. From an overall perspective, the considered WEC prototype has a 1/20th scale model, with the float mass of 3.075 $[kg]$, float moment of inertial (MoI) (at C_g) 0.001450 $[kg \cdot m^2]$, float Draft of $0.11[m]$, float Diameter (at SWL) of 0.256 $[m]$, arm Mass of 1.157 $[kg]$, and arm MoI (at C_g) of 0.0606 $[kg \cdot m^2]$.

As shown in Fig. 2, the floater is connected to a fixed reference frame through two joints (joints A and B) and

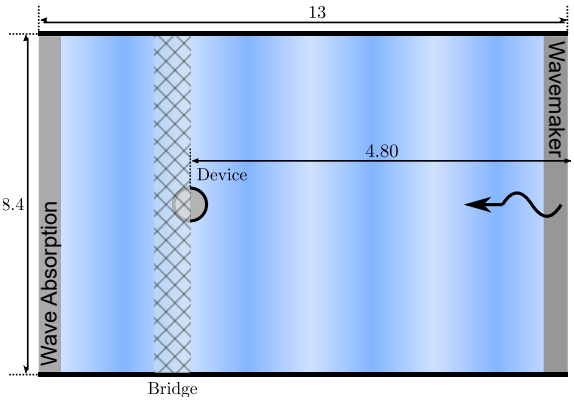

Fig. 3. Schematic of the experimental wave tank for identification tests

a mobile joint (joint C) with a translational displacement indicated by x_m, while the rotational motion is indicated with the angle θ. The position of the PTO system is measured with a position sensor (labelled as 3 in Fig- 2). The floater arm stands at approximately 30° with respect to the horizontal reference plane in its equilibrium position, indicated as still water level (SWL) in Fig. 2. The WEC device is instrumented with a linear motor (equipped with its corresponding driver), acting as a PTO system, a force sensor, a position laser sensor, and an input/output data acquisition board, manufactured by the firm National Instrument. The linear motor and driver are capable of producing a force of up to ± 200 N, which widely covers the purpose of this study. The force sensor is an S-beam Futek LSB302 300lb load cell with SGA Analogue Strain Gauge Amplifier, which represents a high-fidelity force measuring system. The position laser sensor used is a MicroEpsilon ILD-1402-600, also a high-performance system. It must be noted that, although the linear position of the PTO system is measured, the angular position, as considered in the model as output, can be easily derived using basic trigonometric relationships. In addition, due to the structural dimensions and the operational range of the system, the relationship between linear PTO position and the angle of the arm can be effectively approximated by a factor of 5 [19].

The experimental data in this study is acquired during physical wave tank tests in the wave basin at Aalborg University. The tank measures are 13 m in length and 8.4 m in width, with a water depth of 0.9 m. The wave tank is schematically depicted in Fig. 3, including its main dimensions and components. The prototype device is mounted on a supporting structure, which holds a bridge for commissioning and operation, spanning the full width of the tank. The bridge can be seen in Fig. 2, located in the upper-left corner of the picture. The wave tank is instrumented with a wave absorption system to reduce wave reflections, while a wave maker, generally used to generate waves, is also utilised to actively absorb waves and reduce reflections.

A. Force-to-motion experiments

The time-domain force-input experiments are performed over the interval $[0\ 140]$s using linear up-chirp (Eq. 4) experiments in a frequency range of $[0.062875.36]$rad/s, and amplitude set $A_i = \{2.5, 5.0, 7.5, 10.0, 12.5, 15.0, 17.5, 20.0\}$N covering the complete dynamical characterisation of the nonlinear system. Fig. 4 represents the time traces of the reference input force signals ($f_u^\star$), actual force signals (f_u), and angular positions (θ) of all experiments at 8 levels of input amplitude force.

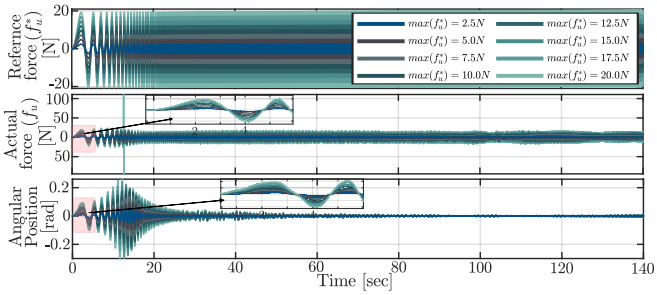

Fig. 4. Time traces of the reference input force ($f_u^\star$) signals, actual force (f_u) signals, and angular position (θ) signals

B. Nonlinearity and noise in time domain data

Through an analysis of the data considering the signals $f_u^\star(t)$, $f_u(t)$, and $\theta(t)$ corresponding to each experiment at different time intervals, (the complete set of data is shown in Fig. 4), the existence of nonlinearities, contamination, and uncertainty sources in the data can be detected, which can be classified in:

1) *Electromechanical effects*: At each amplitude level, a comparison of the reference $f_u^\star(t)$ and actual input forces $f_u(t)$, measured with the load cell, shows the failure of the force control loop (including a PI controller, a linear motor, and a sensor) to track the reference input signal. One of the important aspects contributes to the failure to track the amplitude of the reference signal, which is more significant in experiments with low input amplitude force as depicted in Fig. 5(a) (e.g. 2.5N). The frequency variation of the chirp signal is shown with a red dash-line on the right-hand side of the vertical axis in Fig. 5(a). Another important issue related to the failure of the force control loop is observed in the experiment with the input amplitude level of 20N, where a big jump at the actual input force at the time instance of $t = 12.6$s is observed, illustrated in Fig. 5(b).
   Time-domain analysis of the data also reveals phenomena related to:
   - *Linear motor*: Time-trace analysis of the signals show an operating range of reference input force that produces no response in the actual force, and consequenctly, buoy motion (angular position). This phenomenon known as dead-zone (III-A) in the linear motor, is depicted in Fig. 6(a) and (b) (red highlight), with a comparison of the reference and actual forces on the left-hand

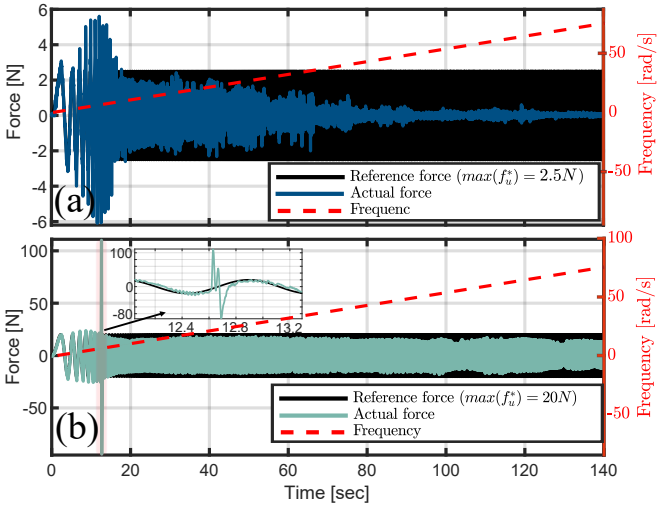

Fig. 5. Input force tracking at amplitude levels of 2.5N and 20N.

vertical axis, and angular position on the right-hand vertical axis for experiments with the lowest (2.5N) and highest (20N) input amplitude forces, respectively. The dead-zone phenomenon is more significant at low input forces. The time interval with no response in the dynamics of the system output (angular position) for the experiments with an amplitude set of A_i is in the set $T_i = \{087, 0.522, 0.425, 0.5, 0.431, 0.33, 0.29, 0.356\}$s.

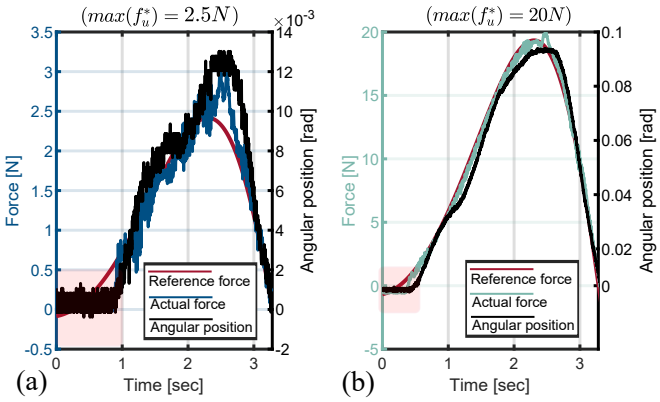

Fig. 6. Dead-zone phenomenon, for the experiments at (a) input amplitude level of 2.5N and (b) input amplitude level of 20N.

Moreover, due to cogging effects, a nonlinear behaviour in the actual input force and consequently in the angular position of the device can be detected presented as a constant or limited response to some operating range of the reference signal. This phenomenon (highlighted in red in Fig. 7) in the time trace of the output signals (angular position) corresponding to the lowest and highest input amplitude forces is represented in Fig. 7, which is more significant (longer time intervals of constant response) in experiments with low input amplitudes.

- *Sensors*: The measured actual input signals ($f_u(t)$) and measured output signals ($\theta(t)$) contain a level of noise that can be possibly contributed to the noise from the sensors during the process of data reading, can be seen through the observation of

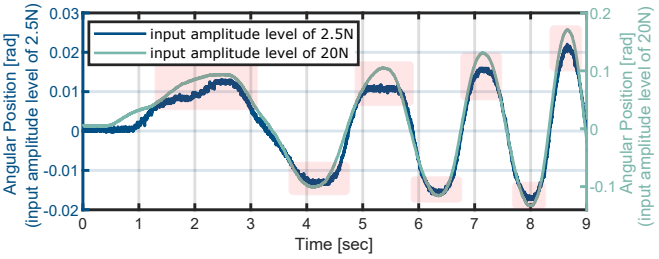

Fig. 7. Cogging effect (saturation-like effect) in the angular position signals of the experiments at input amplitude levels of 2.5 (the blue line with the amplitude shown on the left side of the horizontal axis) and 20N (the green line with the amplitude shown on the right side of the horizontal axis)

.

the actual input signal and output signal in Fig. 6. In experiments with a small input amplitude force (2.5N), the SNR ratio is low and by increasing the input amplitude force, the SNR increases.

2) *Hydrodynamic effects*
Analysis of the time-domain data reveals the movement of the buoy at a range of time intervals where the frequency of the input force is much higher than the resonance frequency of the device and no response in the output is expected. The major phenomenon causing this movement, which is significant in experiments with high input amplitude forces, due to stronger radiated waves, is the wave reflection. The time interval of [130 135]sec of the output signal at input amplitude level of 20N (frequency interval [69.95 72.64]rad/s) is represented in Fig. 8, showing the main sinusoidal signal with the period of approximately 1sec (equivalent to the resonance frequency of the WEC). The additive sinusoidal signal on the main signal will be discussed later.
3) *Structural effects*:
In the experiments, additive sinusoidal oscillations can be observed which is more noticeable in experiments with high amplitude input forces (20N), which can be possibly due to vibrations of the mounting structure. Fig. 8 shows a time interval of [130 135]sec of the angular position of the experiment with the input amplitude force of 20N, where the additive oscillations with the frequency of about 73rad/s, (approximately 11.6 oscillations per second) can be observed.

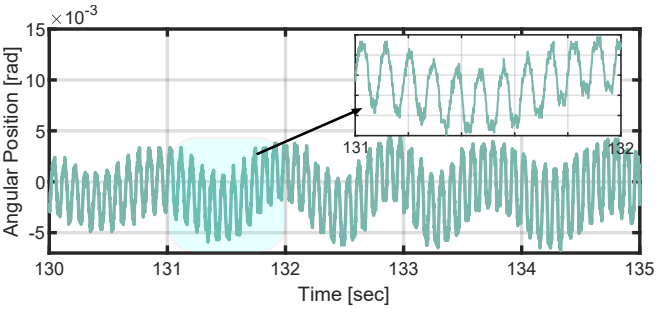

Fig. 8. Observation of wave reflection (frequency of 6.27rad/s) and structural vibration (frequency of 73rad/s) in the output signal of the experiment at amplitude level of 20N.

C. System identification results

System identification results include the calculation of $H_1(j\omega)$ and $H_2(j\omega)$ based on Eq. 3 in Sec. IV. Fig. 9 represents the ETFEs of the first step chain ($H_1(j\omega)$: $f_u^\star(t) \rightarrow f_u(t)$ mapping) based on the block diagram in Fig. 1 at all force input amplitude levels.

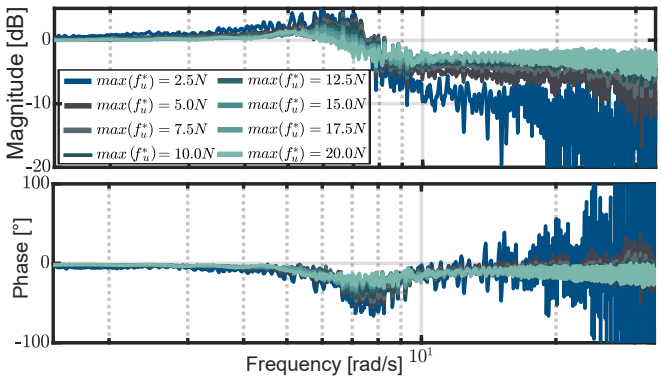

Fig. 9. ETFEs ($H_1(j\omega) : f_u^\star(t) \rightarrow f_u(t)$ mapping) at all input amplitude force levels. (The minimum limit of -20dB on the magnitude axis, and the limit of $[-100\ 100]^\circ$) on the phase axis have been employed to enhance resolution.)

In an ideal case, the magnitude of 0 dB (equal amplitudes of the reference and actual force), and phase of 0° (equal phase components of the reference and actual force) are expected from ($H_1(j\omega)$ results. However, the results of the $H_1(j\omega)$ show the failure of the force control loop both to track the amplitude and phase of the reference force, especially at frequencies higher than 5rad/s. The divergence of the amplitude and phase of $f_u^\star(t)$ from $f_u(t)$ is very significant in experiments with the smallest input amplitude levels and the reference force tracking process is improved at higher input force levels, e.g. 17.5N, 20N.

The next step is the calculation of the ETFEs ($H_2(j\omega) : f_u(t) \rightarrow \theta(t)$ mapping) based on the block diagram in Fig. 1 at all input amplitude levels. Before the calculation of the ETFEs, data pre-processing technique based on the methodology provided in Sec. V-A is applied to the measured output data (angular position) in all of the experiments, using S-G filtering with polynomial order of $N = 4$ (Eq. 5) and frame length of 401 ($M = 200$). The parameters of the filter are tuned to remove the noise from the data in all experiments. The measured output and S-G filtered signals for two experiments with the input force amplitude of 2.5N and 20N are represented in Fig. 10. Based on the results the filtering method perfectly smoothes the time-domain signal from sensor noise which is more significant in terms of SNR in experiments at the input amplitude level of 2.5N. Moreover, applying the S-G filter in the output data of the experiments at the input amplitude level of 20N compensates the nonlinearity of a saturation-like behaviour that can be seen at the time instance of $t = 12.6$s which can be possibly due to saturation in data reading from the sensors. The failure of the force control loop for generating the reference force input of 20N, in generating a big jump in the actual input force at the time instance of $t = 12.6$s (Fig. 5)(b), possibly corresponds to the big jump in the output of the buoy which is beyond the saturation point of the sensor. One of the most important advantages of the S-G filter is the separation of the components that are most likely related to the vibration of the structure which is more obvious at the final times in the experiments at the input amplitude level of $20N$. It is worth mentioning that S-G filtering cannot compensate for the nonlinearity effects of the signal due to the dead-zone, cogging effect, and the wave reflections.

Fig. 11 represents in the time domain (upper plot), and the frequency domain (bottom plot), perturbation amplitude, and perturbation power, respectively, in experiments at input amplitude levels of 2.5N and 20N. The perturbation has been calculated through the difference between the measured output signal and S-G filtered output signal. At the input amplitude level of 20N, the S-G filter compensates for the sensor measurement noise, nonlinearity due to saturation in data reading of the sensor (at $t = 12.6$s), and structural vibration. The inclusion of the structural vibration can be seen both in the time domain, by the sinusoidal nature of the noise at input amplitude level of 20N (magnification of the signal portion highlighted in red in Fig. 11(a)), and in the frequency domain, by peaks of the perturbation power highlighted in red, at frequency point of harmonics of the resonance frequency of the mounting structure (73.32rad/s), at frequencies of 73.32, 148.38, 217.15, 281.39, and 368.87rad/s.

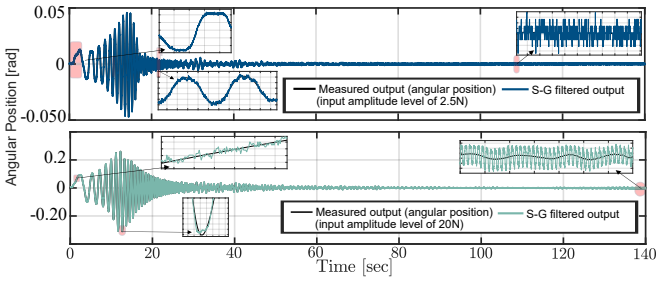

Fig. 10. Measured output signal (angular position) and S-G filtered output signal in experiments with input amplitude levels of 2.5N (upper plot) and 20N (bottom plot).

After the pre-processing of the signal, the ETFEs ($H_2(j\omega) : f_u(t) \rightarrow \theta(t)$ mapping) (Eq. (3)) have been calculated for all the experiments with maximum reference input amplitude level in the set A_i (Sec. VI-A) which is shown in Fig. 12. The actual input forces (f_u) measured by the load cell, and the S-G filtered outputs have been used to calculate the ETFEs. Moreover, phase unwrapping (Sec. V-B) has been applied to compensate the phase jump between the consecutive frequency bins by subtracting 360°. Based on the results of both the magnitude and phase of the ETFEs, fluctuations can be observed that obscure the meaningful information, for instance, the resonance frequency corresponding ETFEs at each level, and the value of the ETFE especially at high-frequency asymptotes. Moreover, in the phase plot of the ETFE, the violation of the passivity by exceeding the limit of -180° at high-frequency asymptotes can be observed. To address these issues, two post-processing techniques have been

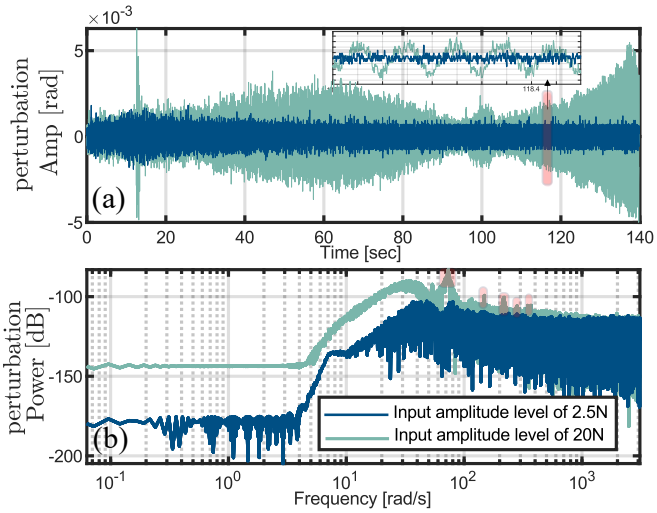

Fig. 11. Perturbation (difference between measured output and S-G filtered output) amplitude and power for the experiments at input amplitude levels of 2.5N and 20N.

employed: *A)* ETFE filtering using moving average (Sec. V-B) for smoothing both the magnitude and phase (in the frequency domain) using 10 number of adjacent data points, and *B)* ETFE phase correction by forcing all the phases in the limit of $[-180\ 0]^\circ$ to guarantee the passivity nature of the WEC. The final ETFEs, after applying the post-processing techniques are represented in Fig. 13. Due to the nonlinearity of the WEC system, different levels of the amplitude of the input signal result in different levels of ETFEs. The major characteristics of ETFEs of this study are consistent with the dynamical characteristics of a WEC system analysed in a NWT setup using the same experiment type (force input amplitudes) in [9], most noticeably, increasing trend of the bandwidth, and a decreasing trend of the peak frequency response (resonance frequency), as the amplitude of the input signal increases. The resonance frequency corresponding to each amplitude level can be obtained by finding the peak point in the magnitude plot or analysing the phase plot where it crosses -90°.

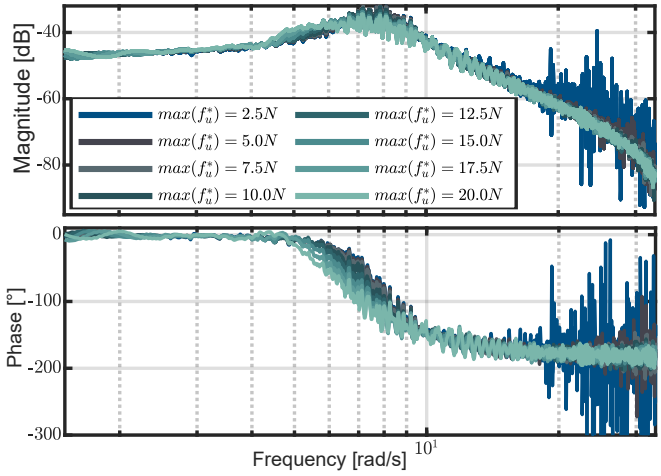

Fig. 12. ETFEs ($H_2(j\omega)$: $f_u(t) \rightarrow \theta(t)$ mapping) at all input amplitude forces after data pre-processing and phase unwrapping post-processing.

To determine a unique nominal model and uncertainty bound for the range of linear models obtained at different amplitude levels of input, the upper and lower limits of the ETFEs ($H_2(j\omega)$) is considered as the uncertainty bounds (black solid-line), and the average of the whole ETFEs has been calculated to obtain the linear nominal model (red solid-line), represented in Fig. 14. The uncertainty bound includes mostly the hydrodynamic uncertainty of the WEC, and the nonlinearity of the WEC model deviated from the nominal WEC model.

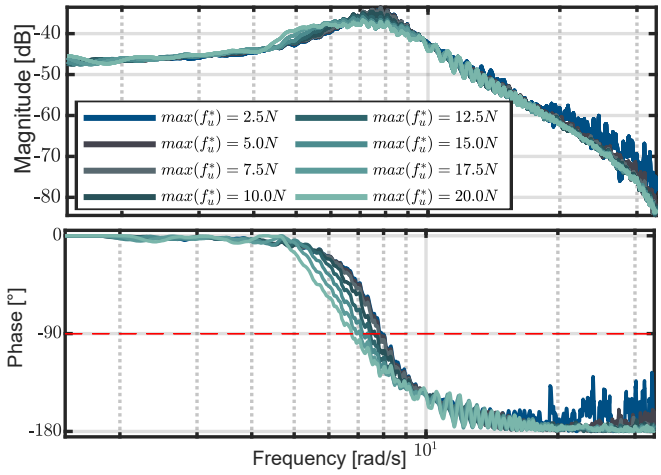

Fig. 13. ETFEs ($H_2(j\omega)$: $f_u(t) \rightarrow \theta(t)$ mapping) at all input amplitude forces after data pre-processing and post-processing (phase unwrapping, passivisation. and moving average filtering).

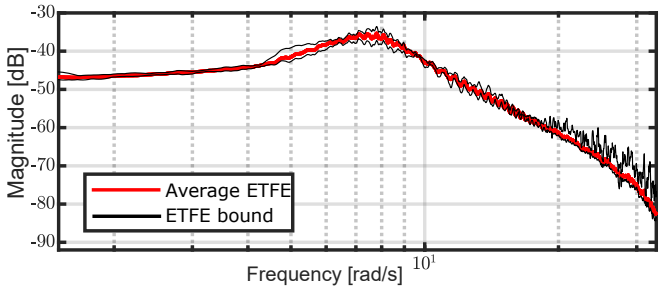

Fig. 14. Nominal model (average of ETFEs at all input amplitude levels) and uncertainty bound.

VII. Perturbation Quantification

This section provides a quantitative measure of the perturbation in the measurements of the wave tank data, including noise, reflection, and structural vibration. To provide a quantitative measure of the noise corresponding to each output signal, the SNR (Eq. 2) is calculated as the ratio of the normalised RMS ($NRMS = RMS/\text{number of samples}$) of the signal to the NRMS of the noise. Since it is difficult to separate noise from other perturbations, in the particular case of this study, the portion of the perturbation signal (Fig. 11) in the time interval of $[60\ 140]s$ from the experiment at the amplitude level of 2.5N has been considered for the calculation of the NRMS of the noise at all experiments, since this time interval includes the most representative white noise corresponding to the measurement noise of the sensors where there is no reflection and structural vibration due to small input amplitude force. Moreover, the movement of the buoy

is almost zero in this time interval. The SNR at all experiments in the units of dB are represented in Fig. 15. The results show that the experiments with low input amplitude forces experience a poor SNR, which might affect the system identification. It is also worth mentioning that the SNR cannot be effectively improved after a certain threshold of the input amplitude force (12.5N).

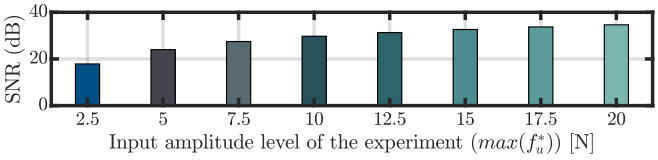

Fig. 15. SNR of the output signals at different levels of input amplitude forces.

Apart from the sensor noise, the other known perturbation sources, wave reflection, and structural vibration have effects on the output signal that can be quantified based on the knowledge of their frequency contents. To this end, the portion of the time domain output signals in the interval of [80 140]s where the frequency of the excitation force is beyond the dynamical range of the device (the buoy movement is due to perturbations), has been considered for all the experiments. The spectral domain analysis of this portion of the time signals shows considerable power with the peaks of the reflection waves (close to the resonance frequency of the device (6.28rad/s)), and resonance frequency of the mounting structure (at 73 rad/s) (Fig. 8). In order to quantify the power corresponding to reflection and structural vibration, band-pass filtering in the frequency domain, with the centre frequency equal to the reflection and resonance frequency of the mounting structure has been applied separately to experiments at all the input amplitude levels. Moreover, the transformation from the frequency domain to the time domain has been applied to get the time domain signals of pure reflection, and structural vibration. The NRMS (from the time domain) of the reflection has been calculated at all the experiments represented in Fig. 16(a_1) and the power of the reflection (in the frequency domain) represented in Fig. 16(a_2) (same colour code as Fig. 16(a_1) for experiments at different input amplitude levels). The same analysis for the quantification of NRMS (Fig. 16(b_1)) and power (Fig. 16(b_2)) of the structural vibration have been represented, showing an increasing trend of the NRMS and power of the reflection and structural vibration as the amplitude of the input force increases.

A. Discussion

For the calculation of a realistic hydrodynamic WEC model in an experimental setup, it is of paramount importance to calculate the ETFEs based on the actual force-to-motion mapping, instead of the reference force-to-motion mapping, and exclude the external noise and disturbance as much as possible. For the current study, an example of the ETFEs comparison, calculated using reference input force/measured output, actual input force/measured output, and actual input force/S-G filtered output (most realistic ETFE for WEC hydrodynamic modelling) are represented in Fig. 17. Comparing the ETFEs computed using reference input force/measured output, and actual input force/measured output shows a significant difference in the magnitude and phase of the ETFEs, pointing out how the ETFE (for hydrodynamic description of the system) can be overestimated if the failure of the reference force tracking is ignored (ETFE based on reference input force/measured output best describes the whole system model, including PTO system). Moreover, a comparison of the ETFEs computed using actual input force/measured output, and actual input force/S-G filtered output (most realistic case) points out the difference in the magnitude of the ETFEs at high-frequency asymptote, as a result of using filtering techniques to exclude perturbations in the output signal.

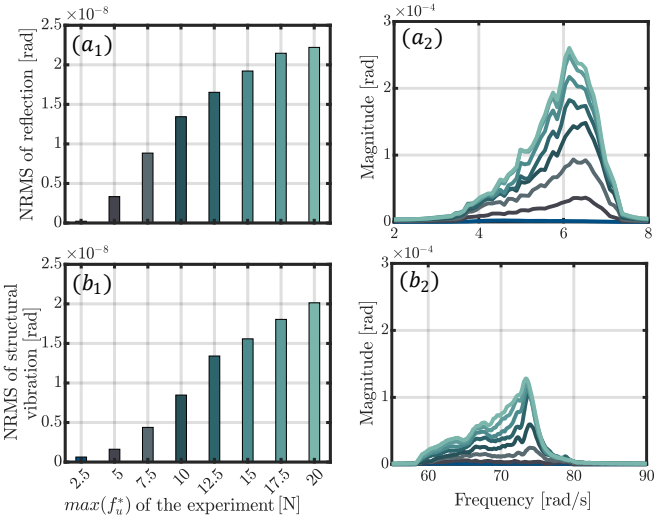

Fig. 16. Power analysis of the reflection and structural vibration: NRMS (a_1) and magnitude (a_2) of the reflection; NRMS (b_1) and magnitude (b_2) of the structural vibration)

It is worth mentioning that, even the most realistic ETFE computed in this case study, does not represent the true behaviour of the WEC hydrodynamics (due to the presence of viscosity, radiated waves, ...), which requires future work on the quantification and separation of nonlinearities and uncertainties not addressed in this study. Moreover, numerical simulation of the same wave tank experiments would provide useful test cases to validate the experimental results.

VIII. Conclusion

The following conclusions can be drawn from the experimental wave tank tests with the analysis of uncertainty and external disturbance sources in wave energy converter modelling:

- The generation of a target force using a force control loop including a PI controller, a linear motor, and a load cell (Fig. 1), fails to accurately track the reference force amplitude and phase (within the frequency range of the excitation force) due to dead-zone effect in the linear motor (no response at the start of the experiment (as evidenced in Fig. 6), contributing to the phase shifting, and flat responses at the extremes (cogging effect, as evidenced in Fig. 7), contributing

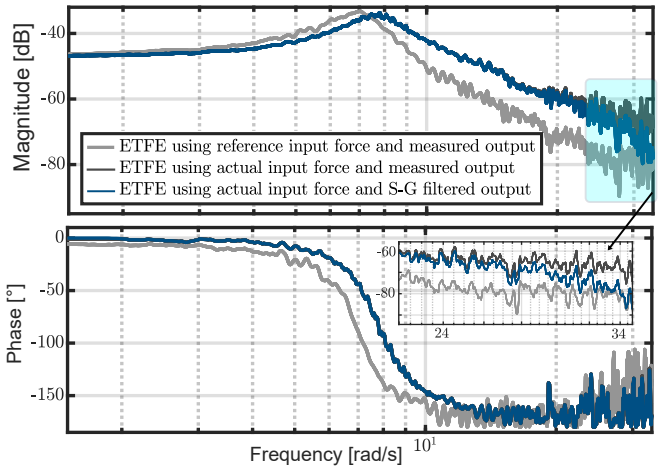

Fig. 17. comparison of the ETFE using actual force-to-motion and reference force-to-motion mapping at the input amplitude level of 2.5N

to the amplitude difference between reference and actual force), the measurement noise from the load cell. The failure of tracking the reference force should be considered specifically in cases of:

1) Calculation of the representative model of the WEC, in using actual force-to-motion mapping for computation of the ETFE instead of reference force-to-motion mapping to get the more accurate amplitude and phase information of the ETFE (articulated in Fig. 17).
2) Consideration of the dead-zone phenomenan of the linear motor, and as a subject for future research, analysis on the compensation for this effect (for instance the method in study [20]) when implementing WEC control strategy. Considering that the force input experiments for the system identification process in this study are basically applied through the PTO system, the same issues could be present in the case of producing control actions through the PTO system in WEC control implementation.

- The quantification, and exclusion of the perturbations from the data of an experimental wave tank test, as much as possible, will result in obtaining representative linear WEC models. High levels of perturbation at the different operating points (input amplitude levels) should be considered carefully, as for example, the dominancy of the noise in small input amplitude force levels may mislead to provide the most representative linear model as per theoretically oscillating in the linear region. Ignoring the possible noise and disturbances can lead to misestimation of the WEC systems modelling, affecting the accuracy of model-based control design, with a consequence on the absorbed power [10].
- The separation of the reference force-to-actual force mapping, and actual force-to-motion mapping, as well as applying the appropriate pre- and post-processing techniques considering the experiment type and input force type, will result in more accurate identification of a representative linear model (beneficial for linear model-based control design) and smaller uncertainty region (beneficial for robust control design).

REFERENCES

[1] M. Penalba, G. Giorgi, and J. V. Ringwood, "Mathematical modelling of wave energy converters: A review of nonlinear approaches," *Renewable and Sustainable Energy Reviews*, vol. 78, pp. 1188–1207, 2017.
[2] M. Farajvand, V. Grazioso, D. García-Violini, and J. V. Ringwood, "Uncertainty estimation in wave energy systems with applications in robust energy maximising control," *Renewable Energy*, vol. 203, pp. 194–204, 2023.
[3] W. Wang, M. Wu, J. Palm, and C. Eskilsson, "Estimation of numerical uncertainty in computational fluid dynamics simulations of a passively controlled wave energy converter," *Proceedings of the Institution of Mechanical Engineers, Part M: Journal of Engineering for the Maritime Environment*, vol. 232, no. 1, pp. 71–84, 2018.
[4] C. Ruzzo, G. Malara, M. Collu, A. Santoro, V. Fiamma, A. Scialò, F. Lagasco, and F. Arena, "Field experiment on a scaled prototype of a floating multi-purpose offshore platform: Dynamic response determination with uncertainty quantification," *Applied Ocean Research*, vol. 129, p. 103402, 2022.
[5] J. Orphin, J.-R. Nader, I. Penesis, and D. Howe, "Experimental uncertainty analysis of an owc wave energy converter," in *12th European Wave and Tidal Energy Conference (EWTEC), Cork, Ireland*, vol. 1, 2017, pp. 1096–1.
[6] P. Lamont-Kane, M. Folley, and T. Whittaker, "Investigating uncertainties in physical testing of wave energy converter arrays," in *Proceedings of the 10th European Wave and Tidal Energy Conference (EWTEC 2013), Aalborg, Denmark*, 2013, pp. 2–5.
[7] W. Qiu, J. S. Junior, D. Lee, H. Lie, V. Magarovskii, T. Mikami, J.-M. Rousset, S. Sphaier, L. Tao, and X. Wang, "Uncertainties related to predictions of loads and responses for ocean and offshore structures," *Ocean Engineering*, vol. 86, pp. 58–67, 2014.
[8] J. Davidson, S. Giorgi, and J. V. Ringwood, "Linear parametric hydrodynamic models for ocean wave energy converters identified from numerical wave tank experiments," *Ocean Engineering*, vol. 103, pp. 31–39, 2015.
[9] M. Farajvand, D. García-Violini, and J. V. Ringwood, "Representative linearised models for a wave energy converter using various levels of force excitation," *Ocean Engineering*, vol. 270, p. 113635, 2023.
[10] D. García-Violini, Y. Peña-Sanchez, N. Faedo, C. Windt, F. Ferri, and J. V. Ringwood, "Experimental implementation and validation of a broadband lti energy-maximizing control strategy for the wavestar device," *IEEE Transactions on Control Systems Technology*, vol. 29, no. 6, pp. 2609–2621, 2021.
[11] Y. Peña-Sanchez, D. García-Violini, and J. V. Ringwood, "Control co-design of power take-off parameters for wave energy systems," *IFAC-PapersOnLine*, vol. 55, no. 27, pp. 311–316, 2022.
[12] D. García-Violini and J. V. Ringwood, "Energy maximising robust control for spectral and pseudospectral methods with application to wave energy systems," *International Journal of Control*, vol. 94, no. 4, pp. 1102–1113, 2021.
[13] W. E. Cummins, "The impulse response function and ship motions," *Schiffstechnik,*, vol. 47, pp. 101–109, 1962.
[14] T. Pérez and T. Fossen, "Time-vs. frequency-domain identification of parametric radiation force models for marine structures at zero speed," *Modeling, Identification and Control*, vol. 29, no. 1, pp. 1–19, 2008.
[15] D. García-Violini, M. Farajvand, C. Windt, V. Grazioso, and J. V. Ringwood, "Passivity considerations in robust spectral-based controllers for wave energy converters," in *2021 XIX Workshop on Information Processing and Control (RPIC), San Juan, Argentina*. IEEE, 2021, pp. 1–6.
[16] M. Penalba and J. V. Ringwood, "A high-fidelity wave-to-wire model for wave energy converters," *Renewable energy*, vol. 134, pp. 367–378, 2019.
[17] A. Savitzky and M. J. Golay, "Smoothing and differentiation of data by simplified least squares procedures." *Analytical chemistry*, vol. 36, no. 8, pp. 1627–1639, 1964.
[18] Wavestar Energy, http://wavestarenergy.com/, 2020, [Online accessed 1-Feb-2020].
[19] M. Kramer, L. Marquis, and P. Frigaard, "Performance evaluation of the Wavestar prototype," in *The 9th European Wave and Tidal Energy Conference (EWTEC), Southampton, UK*, 2011.
[20] J.-S. Mo, Z.-C. Qiu, J.-Y. Wei, and X.-M. Zhang, "Adaptive positioning control of an ultrasonic linear motor system," *Robotics and Computer-Integrated Manufacturing*, vol. 44, pp. 156–173, 2017.